Lab on a Chip

PAPER

Check for updates

Integrated microfluidic three-organ chip for real-time toxicity analysis of fluorotelomer alcohols in the gut–vascular–nerve axis

Xiaodan Ding, Ning Xu, [iD]* Wei Zhang and Peilong Wang*

Perfluoroalkyl substances (PFASs), persistent environmental contaminants linked to neurodevelopmental toxicity, cannot be adequately modeled by traditional *in vitro* systems due to their inability to recapitulate multi-organ interactions. To address this limitation, we developed and engineered a tri-organ gut–vascular–nerve axis chip that reconstructs the bidirectional gut–brain communication through an integrated endothelial barrier. Unlike dispersed 2D cultures on D-polylysine plates, our 3D platform supports cross-linked neurite outgrowth, self-assembled microvascular tubules, and a tightly sealed intestinal epithelia, coupled with integrated solid-phase extraction-mass spectrometry for real-time tracking of PFAS dynamics. We demonstrate that intestinal epithelial cells metabolize fluorotelomer alcohols into bioactive fluorotelomer carboxylic acids, which may transit vascular channels to neural compartments, inducing neuronal dysfunction and driving axis-wide alterations in metabolic activity, oxidative stress responses, and inflammatory signaling. This physiologically relevant model provides novel mechanistic insights into PFAS neurotoxicity and establishes a robust organ-on-chip paradigm for environmental toxicology.

Introduction

Since the 1950s, perfluoroalkyl and polyfluoroalkyl substances (PFASs) have been extensively used in various industrial applications, such as food packaging, textiles, and firefighting foams, due to their remarkable water- and oil-repellent properties.[1,2] However, these substances are highly stable due to the hydrophobic aliphatic chains covalently bonded to fluorine atoms, making them resistant to both chemical and biodegradation. As a result, PFASs have earned the moniker "forever chemicals" and have been detected in numerous environmental matrices, including water, soil, plants, and sludge, as well as in human and animal serum and tissues.[3] Human exposure to PFASs occurs through multiple pathways, including dermal contact, inhalation, and ingestion.[4] Once ingested, PFASs are rapidly absorbed through the gastrointestinal tract, where they enter the bloodstream and are distributed to various tissues, including the blood, liver, kidneys, and reproductive system, where they may exert toxic effects.[5–9] Epidemiological studies have suggested that environmental factors, including PFAS exposure, contribute significantly to human disease and mortality, with estimates indicating that approximately 24% of diseases and 32% of human deaths are linked to environmental pollutants.[10] This

underscores the urgent need for a deeper understanding of the health risks associated with PFAS exposure.

The human brain, with its complex structure and specialized functions, is particularly vulnerable to the toxic effects of environmental pollutants.[11] Numerous studies have highlighted the detrimental effects of PFASs on biological systems, particularly the nervous system, through mechanisms such as oxidative stress and receptor-mediated signaling pathways. Notably, PFAS exposure has been shown to induce neurotoxicity in animal models.[12–17] However, animal experimentation is fraught with significant ethical concerns and is often time-consuming and labor-intensive.[18] Moreover, studying pollutant transport and organ-specific responses remains challenging.[19] The recent shift in regulatory policies, such as the exemption of animal testing before human drug trials in the United States, highlights the growing need for alternative methods to evaluate the effects of environmental pollutants like PFASs on human health.[20]

Microfluidic chips, also known as lab-on-a-chip or cell-on-a-chip platforms, present promising alternatives to traditional methods.[21] These devices offer precise control over cellular microenvironments and fluid flow, enabling the *in vitro* recapitulation of *in vivo* biological processes. They also reduce the need for large sample volumes and reagent costs, making them highly efficient for toxicology and drug efficacy studies.[22] Microfluidic systems can integrate multiple biological components, creating models that replicate tissue interfaces and native microenvironments, thus offering a

State Key Laboratory for Quality and Safety of Agro-Products, Institute of Quality Standards and Testing Technology for Agro-products, Chinese Academy of Agricultural Sciences, Beijing, 100081, China. E-mail: xuning@caas.cn, wangpeilong@caas.cn

more accurate means of studying human diseases and chemical toxicity.[23] However, conventional two-dimensional (2D) co-culture systems are limited by their inability to accurately simulate the adverse effects of harmful environmental factors on humans due to the lack of a physiological microenvironment.[24] While recent advancements have resulted in the development of gut and brain chips for environmental pollutant studies, most of these models focus on a single organ and do not capture the full complexity of pollutant transport and interactions across biological systems.[25–27] Additionally, earlier co-culture platforms involving enterocytes and neurons have not effectively integrated the role of endothelial cells in pollutant transport and regulation, despite improvements in gut–brain communication models.[28,29]

In this study, we present a novel biomimetic and dynamic microfluidic platform designed to investigate the neurotoxic effects of PFAS bioaccumulation within a GVN system. The device consists of a three-dimensional (3D) gel scaffold that supports a venous endothelial cell culture channel, a neuronal cell culture channel, and an intestinal epithelial cell culture channel, arranged in close proximity to mimic in vivo tissue architecture. Interconnecting grooves between the channels promote cellular communication, enhancing the accuracy of modeling the gut–vascular–neural interactions. Furthermore, the system is integrated with an online solid-phase extraction-mass spectrometry (SPE-MS) platform, which enables real-time monitoring of metabolic crosstalk at the gut–vascular–endothelial–neural interface during fluorotelomer alcohol (FTOH) exposure, a representative PFAS compound. Our findings demonstrate that endothelial cells play a critical role in the metabolic transformation of FTOH. After absorption by the intestinal epithelial cells, FTOH is metabolized to produce toxic metabolites, such as fluorotelomer carboxylic acids (FTCAs). These metabolites are then transported through endothelial cells to the neuronal cells, where they induce neurotoxic effects. This study provides new insights into the interaction mechanisms of PFASs within the gut–brain axis and highlights the importance of endothelial cells in mediating the transport and toxicity of environmental pollutants.

Experimental section

Fabrication of the microfluidic chip

The chip model was designed using AutoCAD software, and the microfluidic chip was prepared using traditional soft lithography. The chip was made of PDMS (SYLGARD® 184 Silicone Elastomer Kit) and consisted of three parallel culture chambers and a thin channel in the middle. The three parallel culture chambers were (width 1 mm, length 18.5 mm, height 0.1 mm) connected to each other by 6 thin channels (width 0.15 mm, length 0.5 mm, height 0.1 mm) on both sides of the culture chambers. The three parallel culture chambers were used for the three-dimensional culture and formation of intestinal, vascular and brain organoids. The

inlet and outlet holes with a diameter of 0.75 mm were made with a sharp needle. The chip culture chamber was filled with a cell culture medium. The thin channel in the center was a connection channel for communication between different types of cells. A 10:1 (w/w) PDMS prepolymer of a mixture of PDMS precursor and curing agent was poured onto the template and cured at 85 °C for 4 h to obtain a fully cross-linked PDMS replica mold. After drilling and plasma treatment, the PDMS was bonded to a glass slide and cured at 85 °C for 3 h. Finally, the chip was cleaned with anhydrous ethanol and UV sterilized to maintain sterility until use.

Cell culture

HT-22, HCT116, and HUVEC were purchased from the Institute of Basic Medical Sciences, Chinese Academy of Medical Sciences (Beijing, China). The basal culture medium for HUVEC and HCT116 was Dulbecco's modified Eagle's medium (DMEM, Corning) supplemented with 10% v/v fetal bovine serum (FBS, Corning) and 1% v/v antibiotic solution ($10\,000$ IU mL^{-1} penicillin and 10 mg mL^{-1} streptomycin (Gibco)). The culture medium for HT-22 was a neurobasal medium (Gibco) supplemented with 2% B-27 supplement (FBS, Corning), 1% v/v antibiotic solution ($10\,000$ IU mL^{-1} penicillin and 10 mg mL^{-1} streptomycin (Gibco)), and 1% GlutaMax.

Body-on-a-chip system operation

First, the chip was sterilized with UV light for 30 min, loaded with 0.1% polylysine, incubated on the right side of the channel for 15 min, and rinsed three times with sterile water. Next, the cells in T25 flasks were harvested with trypsin, and HUVEC and HT-22 were incubated with Matrigel (2.5 mg mL^{-1} type IV collagen, ≥5.4 mg mL^{-1} laminin, ≥0.72 mg mL^{-1} entactin, ≤125 µg mL^{-1} ABW, 0827065, Shanghai) and they were mixed and injected into the middle channel and the left channel at a volume of about 1×10^6 and 2×10^6 cells per mL, respectively. It is worth noting that this process was performed on ice. The inoculated microfluidic chip was placed in an incubator to solidify. In addition, HUVEC, HT-22, and HCT116 on-chip monoculture and co-culture were also performed for control. After 24 h, HCT116 at a concentration of approximately 5×10^6 cells per mL was introduced into the right channel and positioned vertically at a 90° angle for 10 min. Finally, the chip was placed on a custom-built device set at a 30° tilt and incubated in an incubator.

PFAS exposure experiments on the microchip

For pollutant stimulation of co-cultures and mono-cultures, FTOH (50 ppm) in freshly supplemented DMEM was introduced into HCT116 channels. After 12 h, the culture medium was removed from the "other tissue" chamber of the system fluid circuit for inflammatory factor measurement and permeability characterization.

Immunofluorescence microscopy analysis

The cells on the chip were fixed with 4% paraformaldehyde for 15 min and then washed with PBS. Immunostaining was performed after permeabilization and blocking for 1 h. The antibodies used in this study are listed in Table S2, and they were incubated on the chip overnight at 4 °C. Subcellular organelles were then labeled using fluorescently conjugated secondary antibodies with VE-Cadherin and β3-tubulin labeling kit (Cell Signaling Technology, Inc.), and cell nuclei were counterstained with 4,6-diamidino-2-phenylindole dihydrochloride (DAPI, Invitrogen). Confocal images were obtained using a microscope (Olympus, Japan, LSM980 Airyscan2, Carl Zeiss, Germany), optical and fluorescence images were obtained using an inverted microscope (Olympus, CKX53), and images and data were analyzed using ImageJ software or ZEN 3.7 software (Carl Zeiss, Germany). The results with error bars are expressed as mean ± standard deviation (SD). Statistical comparisons were performed using one-way analysis of variance (ANOVA), with $P < 0.05$ considered statistically significant.

Analysis of FTOH metabolites

The culture medium was injected into the microchip using a micro-syringe and pump system and connected to the microchannel using Tygon tubing (Fig. S1). The culture medium and FTOH were continuously injected into the microchannel containing cells at a flow rate of 20 μL h^{-1} for incubation. The microchannel outlet of the liquid was collected into a micro-glass tube for metabolite detection. An automatic probe equipped with a modified UPLC syringe was used for precise sampling, and the relevant software could accurately control the sampling position and height. The automatic probe was responsible for transferring the cell metabolite sample from the microtube to the integrated solid phase extraction column, where the sample was loaded, washed, eluted, and finally drained to the analytical column for subsequent analysis (Fig. S1). The chip-SPE-MS platform can realize automated pretreatment of samples. A triple quadrupole mass spectrometer (Shimadzu 8050) was used for multiple reaction monitoring. In particular, the addition of a trapping column in the mobile phase can effectively reduce the background interference of fluoride in the solvent. This system has been successfully applied to the monitoring of cell metabolic dynamics under FTOH exposure conditions.

Results and discussion

Microfluidic chip for the gut–vascular–nerve coculture

The gut is a major target organ for exogenous environmental pollutants. However, increasing evidence suggests that the nervous system also plays a crucial role in mediating the effects of FTOH exposure, particularly in hospitalized patients (Fig. 1A). To explore the impact of FTOH on the brain following intestinal absorption and its subsequent metabolism *via* vascular transport, we developed a
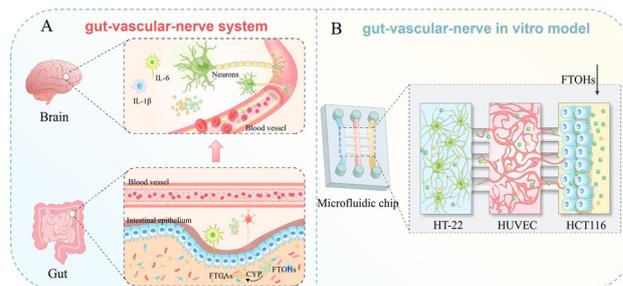

Fig. 1 Microfluidic chip-based gut–vascular–nerve coculture system for real-time monitoring of FTOH biotransformation. (A) Schematic illustration of the gut–vascular–nerve system. (B) Microchip design and schematic diagram of the coculture system consisting of enterocytes, vascular endothelial cells, and neurons.

comprehensive gut–vascular–neural model. This model effectively recapitulates the key physiological features of the gut–brain axis in a controlled and relevant manner. The microfluidic chip consists of three parallel channels representing the intestinal epithelium, vascular endothelium, and neuronal tissue. In this setup, HCT116 and HT-22 were seeded on opposite sides of the HUVEC layer, mimicking the vascular interface (Fig. 1B). To facilitate cellular communication, a membrane-free design was employed, incorporating interconnecting grooves between the channels. This design promotes the growth and migration of vascular microtubule sprouts into both the intestinal and neuronal compartments (Fig. S2), enhancing the intercellular interactions within the system. The compartmentalized structure of the device enables independent control of the three distinct cell types, preserving their unique characteristics and functionality. Endothelial and neuronal cells were cultured with an extracellular matrix (ECM) hydrogel, which was integrated within the chip channels to support cell adhesion and growth. To optimize cellular attachment, the chip, initially filled with HCT116, was tilted at a 30° angle for 5 min, encouraging the cells to adhere to the HUVEC-embedded ECM gel surface. After dynamic culture for 24–48 h, the microfluidic chip was ready for a range of analyses, including imaging, biochemical assays, and functional testing. This innovative platform offers a promising model for studying the interaction between the gut, vascular, and neuronal systems under conditions of FTOH exposure, providing valuable insights into the broader implications of environmental pollutant toxicity on human health.

Formation of 3D neural and vascular networks in a microfluidic chip with ECM hydrogel optimization

Neurons establish complex networks through the extension of their cell bodies, which give rise to axons and dendrites—collectively referred to as "neuronal processes".[30] To better understand how neurons form networks, we optimized the concentrations of ECM hydrogel components for neuronal

cell culture. Based on prior studies, we selected 10%, 20%, and 30% Matrigel for use in a microfluidic chip model.[4] HT-22, mixed with Matrigel, were loaded into the leftmost channel and cultured for 12 h.

In traditional 2D cultures on poly-L-lysine-coated channels, neurons adhered in a random pattern, with minimal network formation. In contrast, when cultured in a 3D environment, the neurons formed a more structured, honeycomb-like microtubule network, exhibiting significantly higher network density. This enhanced network formation can be attributed to cell–matrix interactions, wherein neuronal cells adhered to the ECM *via* integrins and actively exerted traction forces to stretch and reorganize the surrounding matrix, resulting in a reticulated architecture. Notably, collective cell migration along collagen fibers was observed, further contributing to the emergence of an interconnected neural network.

Under 2D conditions, neuronal cells remained dispersed, resulting in reduced neurite outgrowth and difficulty initiating network formation. When 10% Matrigel was added, HT-22 showed longer synaptic extensions. At 20% Matrigel, microtubule formation was further enhanced, stabilizing neuronal morphology and increasing β3-tubulin expression. However, when the Matrigel concentration was increased to 30%, the network appeared sparsely distributed, and neuronal development was reduced (Fig. 2). Thus, 20% Matrigel was identified as the optimal concentration for promoting neural network formation. Under this condition, there was a significant increase in branching points, higher β3-tubulin expression, and the formation of a dense microtubule network. These findings suggest that 20% Matrigel offers the best balance for guiding neurons to form robust networks with enhanced structural integrity. Additionally, endothelial cells, along with their tight junctions, represent the foundational morphological structure and the primary conduit through which exogenous compounds can reach the brain. These tight junctions play a critical role in determining the potential for environmental pollutants to induce neuronal injury.[15] Our observations showed that 20% Matrigel not only facilitated the formation of vascular lumens by HUVEC but also promoted higher expression of VE-cadherin, a key marker of endothelial integrity (Fig. S3). This suggests that 20% Matrigel creates an ideal environment for both neuronal and endothelial cell development, making it an optimal condition for modeling the effects of pollutants on the gut–brain axis.

Assessment of FTOH toxicity in the gut–vascular–nerve model

This study investigates the impact of toxicity on cell viability, vascular formation, and specific protein expression. After exposure to the environmental contaminant PFAS, a significant reduction in viable cell numbers was observed on the chip, accompanied by an increase in the number of dead cells, as revealed by fluorescence imaging. Compared to the control group, cell viability in PFAS-treated chips was significantly reduced, indicating a clear toxic effect.
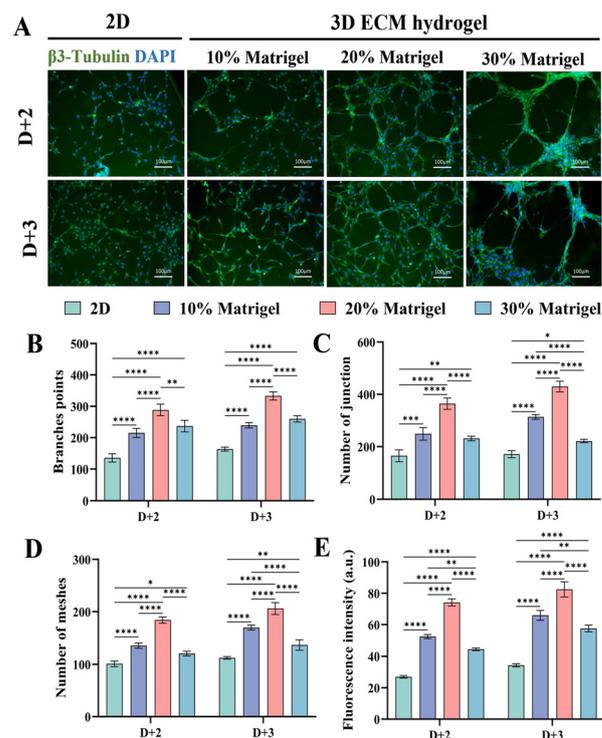

Fig. 2 Optimization of 3D extracellular matrix (ECM) hydrogels for neural network formation in a microfluidic chip. (A) Representative fluorescence images of HT-22 in microchannels under different ECM conditions. β3-tubulin (green), DAPI (blue). (B) Quantification of the number of branches, (C) junctions, and (D) meshes in the HT-22 vasculature at each time point post-culture (n = 5–8, regions of interest (ROIs)). (E) Fluorescence intensity of β3-tubulin under varying ECM conditions in the chip. Statistical analysis was performed using two-way ANOVA followed by Tukey's multiple comparison test. Data are expressed as mean ± SD. *$p < 0.05$, **$p < 0.01$, ***$p < 0.001$, ****$p < 0.0001$.

Interestingly, no significant difference was observed in the total area of the cell lumen before and after exposure to FTOH. However, both the length and number of vascular sprouts, as well as neural axons, were significantly reduced, suggesting that FTOH exposure inhibited the formation of vascular lumens and neural networks (Fig. S4). As shown in Fig. 3A, cells from the control group, including intestinal, endothelial, and neuronal cells, displayed an ordered, tightly packed, and interconnected morphology. In contrast, cells exposed to high concentrations of FTOH became irregular, dispersed, and disorganized. Additionally, the expression patterns of F-actin and DC10 revealed that intestinal differentiation was disrupted following FTOH exposure. The addition of FTOH significantly increased the expression of DC10 in intestinal cells, potentially due to an active response to oxidative stress. Notably, FTOH exposure induced the generation of reactive oxygen species (ROS), which in turn affects actin polymerization and the cellular actin cytoskeleton. This led to an increase in F-actin expression, as shown in Fig. 3B. These findings highlight how FTOH-induced oxidative stress can disrupt cellular structures and
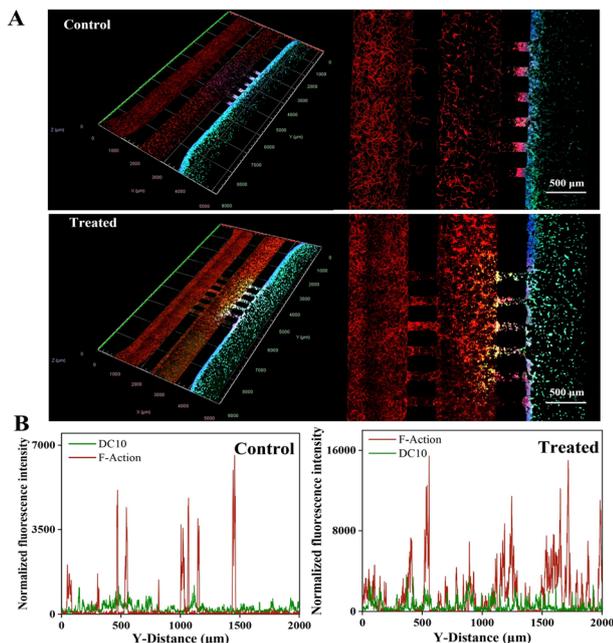
Fig. 3 Effects of FTOH exposure on the gut–vascular–nerve coculture. (A) Immunofluorescence images of DC10 (green) and F-actin (red) after 24 h of high FTOH exposure. (B) The fluorescence intensity along the *Y*-axis of immunofluorescence images of DC10 and F-actin.

Fig. 4 Response of gut–vascular–nerve coculture to FTOH treatment. (A) The expression of IL-6; (B) the expression of IL-1β. **$p < 0.01$, ***$p < 0.001$, ****$p < 0.0001$; (C) the ROS generation after pollutant exposure.

inhibit normal cellular functions, particularly in the context of tissue and network formation.[31]

Subsequently, the impact of environmental pollutants on intestinal permeability was investigated. After PFAS exposure, the amount of dextran in the HUVEC chambers was measured. Time-lapse imaging revealed that over time, small fluorescent molecules migrated from the intestinal layer into the vascular lumen (Fig. S5A). This migration resulted in a significant reduction in calculated permeability, indicating that PFAS exposure compromised the structural integrity and function of the intestinal barrier (Fig. S5B).

Further, we examined the changes in inflammatory cytokine levels (IL-6 and IL-1β) before and after PFAS exposure. The results demonstrated that the secretion of these cytokines was significantly elevated in HCT116, HUVEC, and HT-22 following exposure to the environmental pollutant, compared to the control group. Notably, the secretion of inflammatory cytokines in co-cultured HCT116, HUVEC, and HT-22 was significantly higher than that in monocultured cells, with a marked difference (Fig. 4). This difference is likely due to the role of endothelial cells in mediating intercellular interactions within the co-culture system, resulting in a more complex immune response.[32,33]

ROS, as a key signaling molecule in the progression of inflammation, was further measured using the DCFH-DA probe. Compared to the control group, FTOH treatment induced an increase in ROS generation in HCT116, HUVEC, and HT-22. Interestingly, after FTOH treatment, the fluorescence signal in HT-22 and HUVEC was weaker than
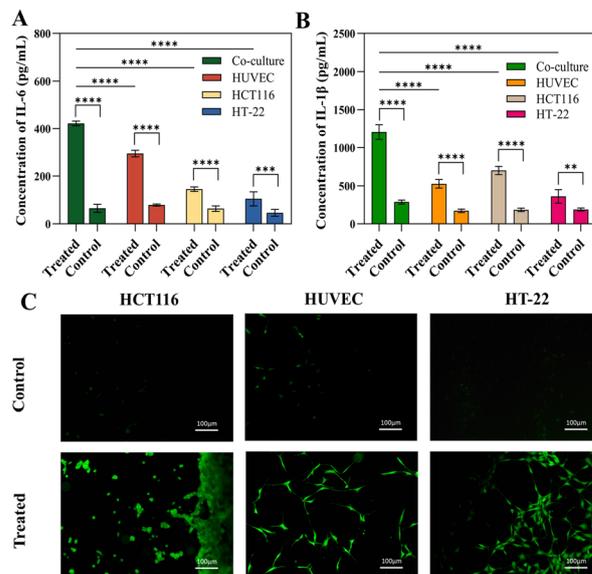
that in HCT116, which further corroborates the differences in barrier function and intercellular interactions (Fig. 4C).

In conclusion, the intestinal–vascular endothelial–neuronal system enables the visualization and quantitative analysis of key biological events influenced by environmental pollutants affecting the gut–brain axis, such as cell death, barrier dysfunction, inflammation, oxidative stress, and changes in specific protein expression. This platform may serve as a valuable tool for environmental toxicology research.

Analysis of gut–vascular–nerve metabolic crosstalk induced by polyfluoroalkyl exposure

The toxicokinetic properties of persistent organic pollutants, particularly PFASs, play a crucial role in their distribution and bioaccumulation within biological systems. These pollutants are first absorbed and partially metabolized in the gut, then enter the bloodstream, pass through the vascular endothelium, and eventually accumulate in brain tissue. However, the impact of the gut–brain axis on PFAS bioaccumulation remains largely unknown. The vascular system is essential for the direct and rapid exchange of molecules between the gut and the brain.[34] To investigate the role of the blood vessels in the absorption, transport, and metabolism of PFASs, a gut–vascular–nerve co-culture model was established using a microfluidic chip. This model simulates the interaction mechanisms involved in the transport and metabolism of PFASs in enteric neuronal cells and was used to evaluate the effects of PFAS exposure.

To explore the differences in target metabolism among various cell types, online monitoring of FTOH oxidation was
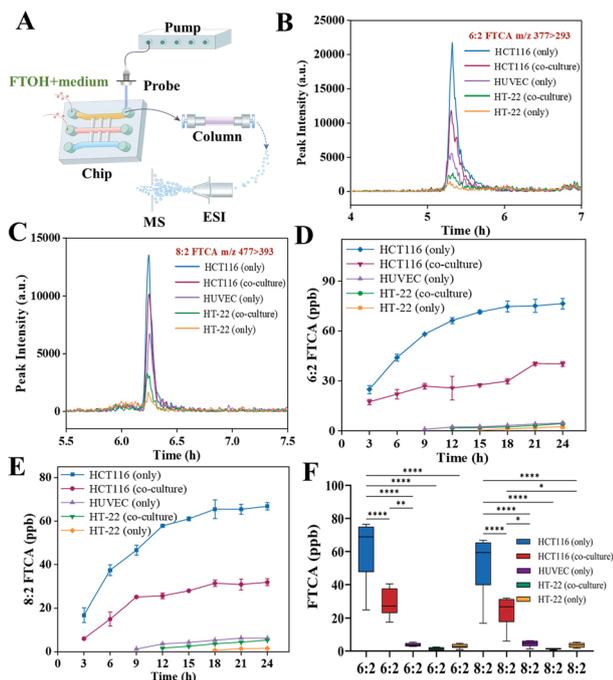
Fig. 5 Dynamic monitoring of 6 : 2 and 8 : 2 FTOH in coculture and monoculture systems. (A) Schematic representation of the coculture chip coupled with solid-phase extraction mass spectrometry (SPE-MS). The HCT116 channel was perfused with the culture medium and FTOHs at 5 μL min^{-1}, while the HT-22 channel was perfused with the culture medium alone at the same flow rate. Metabolites were sampled from the pooled channels of either the HCT116 or HT-22 lines. (B) Ion chromatograms of the metabolic compound 6 : 2 FTCA. (C) Ion chromatograms of the metabolic compound 8 : 2 FTCA. (D) Time-dependent formation of 6 : 2 FTCA. Data were analyzed using spline fitting. (E) Time-dependent formation of 8 : 2 FTCA. Data were analyzed using spline fitting. (F) Statistical analysis of the data shown in panels (D) and (E) was performed using one-way ANOVA followed by Tukey's multiple comparison test. $*p < 0.05$, $**p < 0.01$, $***p < 0.001$, $****p < 0.0001$. Data are expressed as mean ± SD from at least three independent experiments.

conducted using SPE-MS (Fig. 5A). Upon exposure to environmental pollutants, FTOH was transported to the gut, where it underwent biotransformation. This process led to the formation of the more toxic metabolite, FTCA, through CYP450-mediated oxidative metabolism. RT-PCR analysis of several CYP isoforms revealed that CYP1A1, CYP1A2, CYP3A4, CYP3A5, CYP1B1, CYP2C19, CYP2C9, and CYP2E1 were highly expressed in the gut, with CYP1A2 and CYP2E1 identified as key metabolic enzymes (Fig. S6). These findings suggest that the gut plays a primary role in the metabolism of exogenous environmental pollutants in this model. Continuous incubation of FTOH led to intestinal barrier dysfunction, which allowed FTOH and its metabolites to diffuse into the intermediate HUVEC channel and subsequently into the HT-22 channel, resulting in neurotoxicity. The metabolites 6 : 2 FTCA and 8 : 2 FTCA were quantified by mass spectrometry, with calibration curves established for each (Fig. S7).

The time-dependent metabolism of environmental pollutants is crucial for understanding their toxicokinetics. As shown in Fig. 5, when cells were incubated with 50 ppm FTOH, the concentration of FTCA metabolites in HCT116 continuously increased over time, with FTCA production starting around 18 hours and quickly reaching saturation. However, the metabolite levels in the co-culture system were lower, suggesting that HUVEC may regulate the absorption and metabolism of FTOH. The reduced production of metabolites in HT-22 and HUVEC could be due to lower expression of CYP enzymes in these cell types. A comparison of FTOH metabolism between co-culture and monoculture conditions revealed significant differences, further highlighting the role of endothelial and neuronal interactions in modulating pollutant metabolism.

Conclusions

In this study, we developed a microfluidic co-culture platform that models the gut–brain axis by integrating a three-dimensional vascular network within a parallel-channel microfluidic architecture. The system incorporates discrete but interconnected channels for intestinal epithelial cells, vascular endothelial cells embedded in a 3D hydrogel scaffold, and neuronal cells, thereby recreating key structural and functional features of the *in vivo* gut–vascular–neural interface. Leveraging this chip-based platform, we established an environmental toxicology model capable of visualizing and quantifying PFAS-induced neurotoxicity, including barrier disruption, oxidative stress, and inflammation. To probe the biotransformation dynamics of FTOH, we employed on-chip solid-phase extraction coupled with mass spectrometry for real-time metabolic analysis. Notably, the co-culture model exhibited a reduced accumulation of FTCA compared to single-cell-type cultures, suggesting a modulatory role of vascular endothelial cells in the metabolic interplay between intestinal and neuronal compartments. This work underscores the value of integrated organ-on-chip systems for elucidating inter-organ toxicological mechanisms of environmental pollutants.

Conflicts of interest

The authors declare no competing financial interest.

Data availability

The data supporting the findings of this study are available from the Institute of Agricultural Quality Standards and Testing Technology, Chinese Academy of Agricultural Sciences. However, access to these data is restricted, as they were used under license for the current study and are not publicly available.

Supplementary information is available. See DOI: **https://doi.org/10.1039/d5lc00631g**.

Acknowledgements

References

1 S. Bhardwaj, M. Lee, D. O'Carroll, J. McDonald, K. Osborne, S. Khan, R. Pickford, N. Coleman, C. O. Farrell, S. Richards and M. J. Manefield, *J. Hazard. Mater.*, 2024, **478**, 135510.

2 K. M. Ríos-Bonilla, D. S. Aga, J. Lee, M. König, W. Qin, J. R. Cristobal, G. E. Atilla-Gokcumen and B. I. Escher, *Environ. Sci. Technol.*, 2024, **58**(38), 16774–16784.

3 A. Di Nisio, M. Pannella, S. Vogiatzis, S. Sut, S. Dall'Acqua, M. S. Rocca, A. Antonini, A. Porzionato, R. De Caro, M. Bortolozzi, L. D. Toni and C. Foresta, *Environ. Int.*, 2022, **158**, 106982.

4 N. Xu, H. Lin, J.-M. Lin, J. Cheng, P. Wang and L. Lin, *Anal. Chem.*, 2023, **95**, 17064–17072.

5 N. Caporale, M. Leemans, L. Birgersson, P.-L. Germain, C. Cheroni, G. Borbély, E. Engdahl, C. Lindh, R. B. Bressan and F. Cavallo, *et al.*, *Science*, 2022, **375**, eabe8244.

6 J. Li, L. Wang, X. Zhang, P. Liu, Z. Deji, Y. Xing, Y. Zhou, X. Lin and Z. Huang, *Sci. Total Environ.*, 2022, **852**, 158362.

7 K. Roth, Z. Yang, M. Agarwal, W. Liu, Z. Peng, Z. Long, J. Birbeck, J. Westrick, W. Liu and M. C. Petriello, *Environ. Int.*, 2021, **157**, 106843.

8 K. R. Taibl, S. Schantz, M. T. Aung, A. Padula, S. Geiger, S. Smith, J.-S. Park, G. L. Milne, J. F. Robinson, T. J. Woodruff, R. Morello-Frosch and S. M. Eick, *Environ. Int.*, 2022, **169**, 107541.

9 L. You, J. Kou, M. Wang, G. Ji, X. Li, C. Su, F. Zheng, M. Zhang, Y. Wang and T. Chen, *et al.*, *Nat. Commun.*, 2024, **15**(1), 2268.

10 X.-y. Du and J.-y. Yang, *Sci. Total Environ.*, 2024, **919**, 170745.

11 M. Y. Xie, Z. Y. Lin, X. F. Sun, J. J. Feng, L. Mai, C. C. Wu, G. L. Huang, P. Wang, Y. W. Liu and L. Y. Liu, *et al.*, *Environ. Int.*, 2024, **187**, 108719.

12 B. Bharal, C. Ruchitha, P. Kumar, R. Pandey, M. Rachamalla, S. Niyogi, R. Naidu and R. K. Kaundal, *Sci. Total Environ.*, 2024, **955**, 176941–176941.

13 W. Hu, M.-Y. Zhang, L.-Y. Liu, Z.-F. Zhang and Y. Guo, *J. Hazard. Mater.*, 2023, **442**, 130003.

14 Y. Xia, J. Chen, P. Dong, L. Zhang, Y. Ding, W. Ding, X. Han, X. Wang and D. Li, *Mol. Neurobiol.*, 2024, **62**(4), 4203–4220.

15 Y. Xia, Y. Chen, J. Chen, X. Han, X. Wang and D. Li, *Environ. Chem. Lett.*, 2024, **22**, 967–973.

16 M.-Y. Xie, Z.-Y. Lin, L.-Y. Liu, C.-C. Wu, Y.-W. Liu, G.-L. Huang and E. Y. Zeng, *Environ. Res.*, 2022, **204**, 112011.

17 H.-Y. Zhuchen, J.-Y. Wang, X.-S. Liu and Y.-W. Shi, *Toxics*, 2023, **11**, 571.

18 H.-Y. Tan, H. Cho and L. P. Lee, *Nat. Biomed. Eng.*, 2021, **5**, 11–25.

19 S. Yang, T. Zhang, Y. Ge, Y. Cheng, L. Yin, Y. Pu, Z. Chen and G. Liang, *J. Hazard. Mater.*, 2023, **458**, 131962.

20 M. Wadman, *Science*, 2023, **379**, 127–128.

21 S. E. Park, A. Georgescu and D. Huh, *Science*, 2019, **364**, 960–965.

22 M. Schultze, M. Fieß, N. Karpowicz, J. Gagnon, M. Korbman, M. Hofstetter, S. Neppl, A. L. Cavalieri, Y. Komninos and T. Mercouris, *et al.*, *Science*, 2010, **328**, 1658–1662.

23 J. Ahn, K. Ohk, J. Won, D.-H. Choi, Y. H. Jung, J. H. Yang, Y. Jun, J.-A. Kim, S. Chung and S.-H. Lee, *Nat. Commun.*, 2023, **14**(1), 1488.

24 C. Hu, S. Yang, T. Zhang, Y. Ge, Z. Chen, J. Zhang, Y. Pu and G. Liang, *Environ. Int.*, 2024, **184**, 108415.

25 L. C. Delon, M. Faria, Z. Jia, S. Johnston, R. Gibson, C. A. Prestidge and B. Thierry, *Small Methods*, 2023, **7**(1), 2200989.

26 S. Jalili-Firoozinezhad, R. Prantil-Baun, A. Jiang, R. Potla, T. Mammoto, J. C. Weaver, T. C. Ferrante, H. J. Kim, J. M. S. Cabral, O. Levy and D. E. Ingber, *Cell Death Dis.*, 2018, **9**, 223.

27 Y. Q. Wang, L. Wang, Y. J. Zhu and J. H. Qin, *Lab Chip*, 2018, **18**, 851–860.

28 M.-H. Kim, D. Kim and J. H. Sung, *J. Ind. Eng. Chem.*, 2021, **101**, 126–134.

29 X. Li, E. K. He, G. Q. Chen, X. D. Cao, L. Zhao, X. Y. Xu, Z. Z. Fu and H. Qiu, *Environ. Int.*, 2024, **192**, 109026.

30 J. A. Pradeepkiran, P. Rawat, A. P. Reddy, E. Orlov and P. H. Reddy, *Neural Regener. Res.*, 2025, **20**, 2624–2632.

31 C. Rouyère, T. Serrano, S. Frémont and A. Echard, *Eur. J. Cell Biol.*, 2022, **101**, 151249.

32 J. Amersfoort, G. Eelen and P. Carmeliet, *Nat. Rev. Immunol.*, 2022, **22**, 576–588.

33 A. M. Padmanaban, K. Ganesan and K. M. Ramkumar, *Bioengineering*, 2024, **11**, 1090.

34 S. Carloni and M. Rescigno, *Semin. Immunopathol.*, 2022, **44**, 869–882.